LETTER

doi:10.1038/nature19842

Magnetic reversals from planetary dynamo waves

Andrey Sheyko[1], Christopher C. Finlay[2] & Andrew Jackson[1]

A striking feature of many natural dynamos is their ability to undergo polarity reversals[1,2]. The best documented example is Earth's magnetic field, which has reversed hundreds of times during its history[3,4]. The origin of geomagnetic polarity reversals lies in a magnetohydrodynamic process that takes place in Earth's core, but the precise mechanism is debated[5]. The majority of numerical geodynamo simulations that exhibit reversals operate in a regime in which the viscosity of the fluid remains important, and in which the dynamo mechanism primarily involves stretching and twisting of field lines by columnar convection[6]. Here we present an example of another class of reversing-geodynamo model, which operates in a regime of comparatively low viscosity and high magnetic diffusivity. This class does not fit into the paradigm of reversal regimes that are dictated by the value of the local Rossby number (the ratio of advection to Coriolis force)[7,8]. Instead, stretching of the magnetic field by a strong shear in the east–west flow near the imaginary cylinder just touching the inner core and parallel to the axis of rotation is crucial to the reversal mechanism in our models, which involves a process akin to kinematic dynamo waves[9,10]. Because our results are relevant in a regime of low viscosity and high magnetic diffusivity, and with geophysically appropriate boundary conditions, this form of dynamo wave may also be involved in geomagnetic reversals.

Motion of liquid metal in Earth's core is the source of the geomagnetic field and its time variations, including dramatic polarity reversals wherein the large-scale field switches to point in the opposite direction. The past twenty years have seen considerable advances in our ability to model this process, with the advent of 3D numerical geodynamo models capable of solving the equations of conservation of momentum, magnetic induction and buoyancy transport in a self-consistent manner[11,12]. Some such models show polarity reversals[13–15], which proceed by the production and expulsion of inverse magnetic flux by intermittent convective plumes, and subsequent transport by meridional flow[6,16]. By necessity, such simulations operate in a regime in which viscous effects remain important. However, the values of the two dimensionless parameters that characterize these simulations—the Ekman number $\mathrm{Ek}=\nu/(2\Omega d^2)$ and the magnetic Prandtl number $\mathrm{Pr_m}=\nu/\eta$, where ν is the kinematic viscosity, Ω is the angular rotation rate, d is the thickness of the spherical shell of convecting fluid and η is the magnetic diffusivity—differ greatly from the values estimated for Earth's core, and so it is possible that other processes operate under such conditions[17]. Figure 1 summarizes Ek and $\mathrm{Pr_m}$ for a selection of published models that exhibit polarity reversals (see Extended Data Table 1).

In an effort to push towards the low-viscosity regime, some researchers have experimented with stress-free boundary conditions in geodynamo models, and discovered a wide variety of quadrupolar and hemispheric dynamos, some of which undergo prominent field oscillations, excursions and reversals[10,18] via a dynamo-wave mechanism[9]. Dynamo waves have been extensively studied in both 2D and 3D using prescribed flows[2,19,20]; they involve cyclic variations in magnetic induction due to the combined action of differentially rotating (shear) flow and helical flow. Up to now, the relevance of such solutions to Earth has been uncertain because they have been found only in kinematic models, or in dynamic models with unusual boundary conditions or forcing modes. Here, we demonstrate that dynamo waves can also produce polarity reversals in a standard geodynamo model set-up, provided that Ek and $\mathrm{Pr_m}$ are sufficiently small and that the rate of convective driving is sufficiently large.

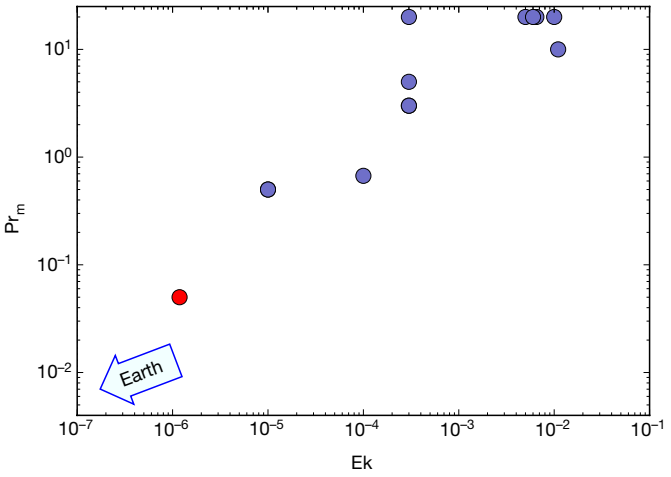

Figure 1 | Control parameters of a selection of numerical geodynamo models that exhibit polarity reversals. The blue dots are the parameters for published reversing-geodynamo models (see Extended Data Table 1). The red dot shows the parameters for the reversing dynamo S6 discussed here. $\mathrm{Ek}=\nu/(2\Omega d^2)$ is the Ekman number and $\mathrm{Pr_m}=\nu/\eta$ is the magnetic Prandtl number, where ν is the kinematic viscosity, Ω is the angular rotation rate, d is the thickness of the spherical shell of convecting fluid and η is the magnetic diffusivity. For case S6, $\mathrm{Ek}=1.2\times10^{-6}$ and $\mathrm{Pr_m}=0.05$. The Earth lies off to the bottom left in this diagram (as indicated by the arrow), with estimated values of $\mathrm{Ek}=\mathcal{O}(10^{-15})$ and $\mathrm{Pr_m}=\mathcal{O}(10^{-5})$.

We adopt a numerical approach to solve the equations governing convection-driven magnetohydrodynamics in a rapidly rotating, electrically conducting, spherical shell (see Methods). The calculations reported here were started from an earlier run with parameters and set-up as close as possible to a previously reported dynamo simulation[21,22], which uses among the smallest published values for Ek (1.2×10^{-6}) and $\mathrm{Pr_m}$ (0.2). In a calculation hereafter referred to as 'S6', the convective driving (as measured by the Rayleigh number Ra; see Equation (2) in Methods) was then increased by a factor of 30 and $\mathrm{Pr_m}$ decreased to 0.05, in an effort to break the strong equatorial anti-symmetry of the generated field and to enhance its time variability. Figure 2a shows that, following the change in the control parameters, there is a gradual decrease in the magnitude of the magnetic energy in dynamo S6. Then, after about 1.1 magnetic diffusion times with a steady, dipole-dominated field, nearly periodic reversals of the dipole field set in (Fig. 2b). The period of the reversals is approximately 0.18 magnetic diffusion times and they persist for the 6 magnetic diffusion times that we have been able to calculate so far. We repeated the calculations with increased model resolution, in both angular and radial directions, and continue to find the same reversing behaviour.

[1]Institute of Geophysics, ETH Zurich, 8092 Zurich, Switzerland. [2]Division of Geomagnetism, DTU Space, Technical University of Denmark, 2800 Kongens Lyngby, Denmark.

© 2016 Macmillan Publishers Limited, part of Springer Nature. All rights reserved.

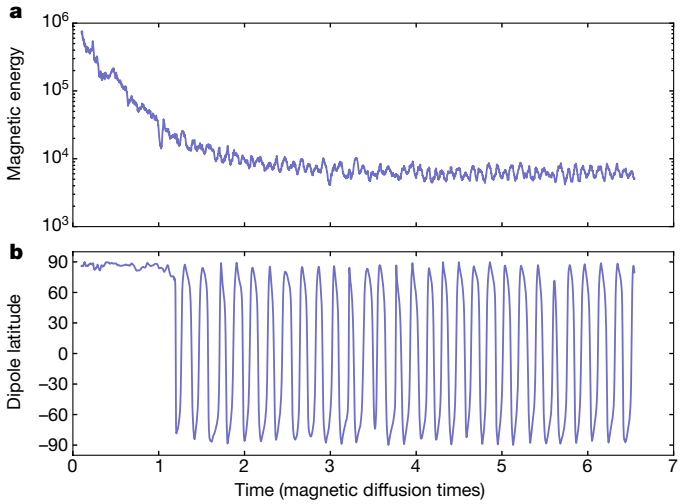

Figure 2 | Magnetic field time-dependence for dynamo S6. a, Time dependence of the magnetic energy, integrated over the volume of the dynamo region, for dynamo S6. The simulation was started from a previous dipole-dominated run similar to the dynamo of ref. 21, then the Rayleigh number Ra was increased by a factor of 30 and the magnetic Prandtl number Pr_m decreased by a factor of 4. **b**, The resultant time dependence of the dipole tilt, determined from the first three Gauss coefficients $\{g_1^0, g_1^1, h_1^1\}$ of the magnetic field at the outer boundary. Polarity reversals set in around 1.1 magnetic diffusion times.

Figure 3 presents the detailed structure and time-dependence of the reversing field in dynamo S6. The radial magnetic field B_r at the outer boundary of the dynamo is primarily axisymmetric, and consists of bands with alternating polarity that appear at low latitude and subsequently move polewards (Fig. 3b, c and Supplementary Video 1). The northern hemisphere field is stronger and migrates polewards more slowly (see the lines in Fig. 3b, which illustrate that the speed dz/dt, where $z = \sin(\lambda)$ and λ is the latitude, is 50% faster in the southern hemisphere). The reversing field at the outer boundary is linked to deep structures that are evident in meridional sections of the longitudinally averaged azimuthal field $\overline{B_\varphi}$ (Fig. 3d and Supplementary Videos 2, 3). In the equatorial plane, the sign of $\overline{B_\varphi}$ alternates, and the field subsequently migrates polewards in each hemisphere, moving parallel to the rotation axis.

In Fig. 4, we examine the underlying flow that generates this distinctive pattern of field reversals. Figure 4a shows the time-averaged kinetic energy spectrum as a function of spherical harmonic degree. The kinetic energy in the reversing regime is much larger than the magnetic energy, and it decays more slowly with spherical harmonic degree. It is nonetheless dominated by degrees below 20, and has a notably large zonal component. Snapshots and animations of the flow (Supplementary Videos 4, 5) reveal columnar flow patterns with strong alignment parallel to the rotation axis, typical of low-Ek rotating convection. The time and longitudinally averaged flow in S6 is presented in Fig. 4b, c, which shows meridional sections of the angular velocity (differential rotation) and radial flow. There is a strong retrograde jet close to the tangent cylinder; this produces substantial shear perpendicular to the rotation axis and is associated with weaker, but persistent, radial flow. There is a surprising difference between the angular velocities in the northern and southern hemispheres: prograde zonal flow at low latitudes in the southern hemisphere is absent in the northern hemisphere. This may be linked to the southern hemisphere being colder at the outer boundary (see Supplementary Video 6). Flow asymmetry between the northern and southern hemispheres, and a substantial quadrupolar component in the generated field, are conditions known to favour reversing behaviour in dynamos[23,24]. Neither the kinetic energy nor the structure of the flows varies much during the reversals.

To further investigate the nature of the reversal process, we carried out a series of additional calculations, in which we varied the control

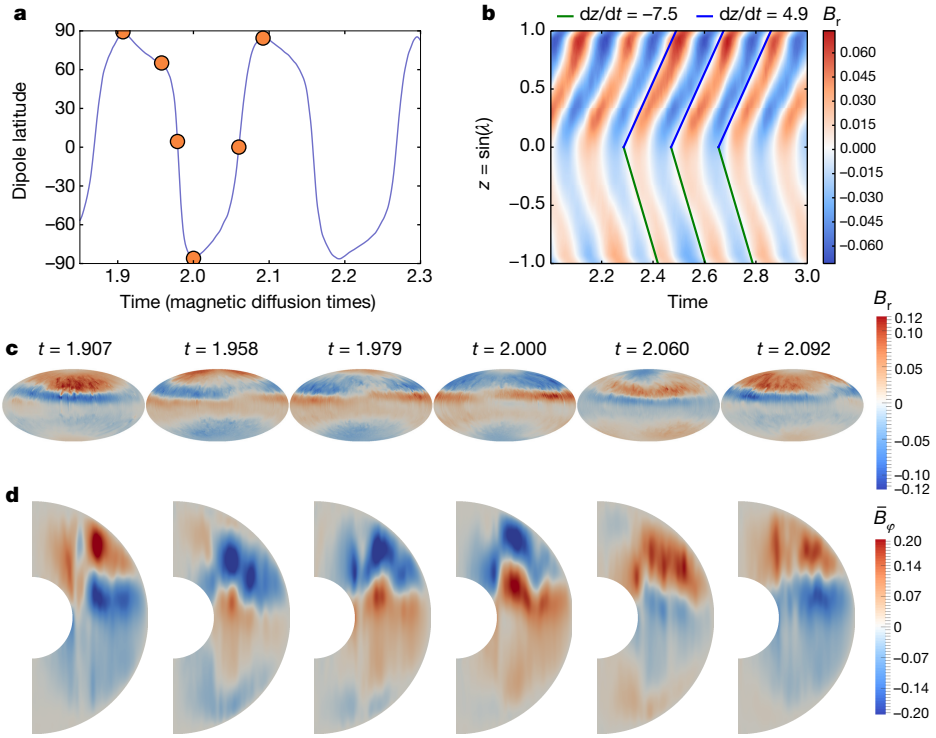

Figure 3 | Magnetic field polarity reversal process. a, A close up of time dependence of the dipole tilt angle from dynamo S6 (Fig. 2b); orange dots mark the time instances shown in **c** and **d**. **b**, A butterfly plot of the longitudinally averaged radial magnetic field B_r at the outer boundary of the dynamo region as a function of $z = \sin(\lambda)$, where λ is the latitude, and time t. **c**, Sequence showing B_r at the outer boundary of the liquid metal region, in a Hammer projection, for the times marked by the orange dots in **a**. **d**, Sequence of meridional sections showing the longitudinally averaged azimuthal field $\overline{B_\varphi}$ within the liquid metal region.

© 2016 Macmillan Publishers Limited, part of Springer Nature. All rights reserved.

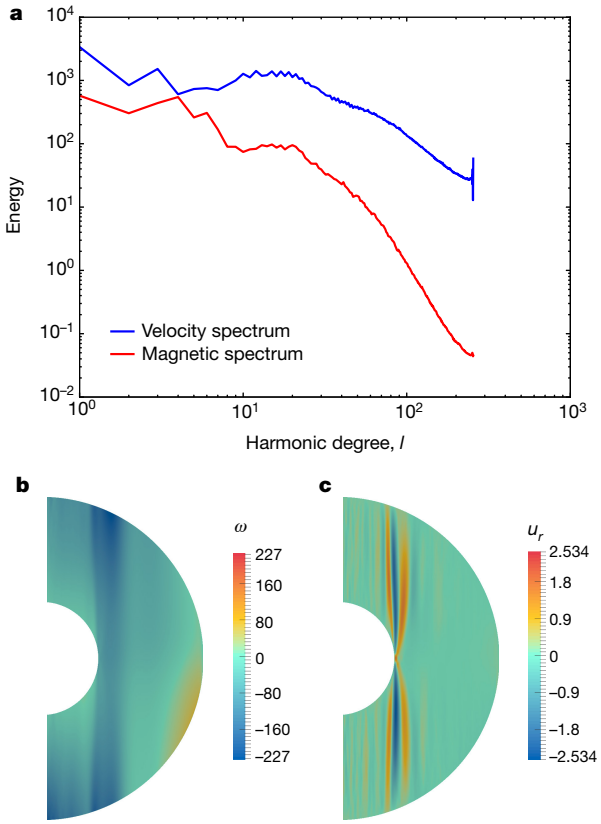

Figure 4 | Time-averaged flow in dynamo S6. a, Volume-averaged spectra of the kinetic energy (blue) compared to the magnetic energy (red), time-averaged over the reversing interval. **b**, A meridional section showing the time and longitudinally averaged angular velocity ω, with blues denoting retrograde velocities and reds denoting prograde velocities. **c**, Similar meridional section for the radial flow (u_r, radial velocity); reds show radially outward flow.

parameters and set-up of the dynamo (see Extended Data Table 2). Upon increasing Ra, which enhances the magnetic Reynolds number Re_m and the amplitude of the zonal flow, we continue to find similar reversals, but with shorter periods and increasing time variability (runs S6.04–S6.08). Decreasing Pr_m much further is difficult without losing the dynamo, but small decreases slightly shorten the reversal period (runs S7.02, S7.03). Replacing the electrically conducting inner core with an insulating inner core makes little difference (the reversal period becomes very slightly shorter; see run S6_InsIC), presumably because the reversals result primarily from processes outside the tangent cylinder. We also carried out one calculation with the Lorentz force switched off (case S6_LorOff). Very similar reversals were then obtained, but with a shorter period of only 0.07 magnetic diffusion times. The helicity of the flow did not change much upon switching off the Lorentz force, but the energy in the zonal part of the toroidal flow increased by a factor of five. A calculation using a revised model '$S6_{\varepsilon 0}$', in which the internal heating is set to zero (and all other parameters remain the same as in S6; see Extended Data Table 2), has established that in this case the dynamo continues to reverse in a similar manner, with its period differing by less than 5% from that of S6 (see Methods).

We next consider whether these reversals can be the result of a dynamo-wave process. A first clue is that Parker's theory[2,9] predicts poleward propagation of dynamo waves along cylinders parallel to the rotation axis, in the case that the magnitude of the (westward) angular velocity decreases with distance away from the tangent cylinder and helicity is negative in the northern hemisphere. This is in agreement with our results. In addition, the period of dynamo waves can be estimated by[10,18]

$$T_{\mathrm{Parker}} = 2\pi\gamma[H(\overline{E_{\mathrm{tor}}})^{1/2}]^{-1/2} \quad (1)$$

where T_{Parker} is the predicted reversal period, γ is a constant, $H = \left|\int_V (\boldsymbol{u}-\overline{\boldsymbol{u}})\cdot\boldsymbol{\nabla}\times(\boldsymbol{u}-\overline{\boldsymbol{u}})\mathrm{d}V\right|$ is the modulus of the volume-integrated kinetic helicity of the non-axisymmetric flow that we evaluate in the northern hemisphere, and $\overline{E_{\mathrm{tor}}}$ is the zonal toroidal flow energy. Both quantities were time-averaged over the reversing interval. Upon comparing the predictions of this theory with the reversal periods found in our numerical calculations (Extended Data Table 2) we find a reasonable agreement (Extended Data Fig. 1), especially regarding the decrease in reversal period as the energy of toroidal zonal flow increases.

Dynamo S6 thus demonstrates that field oscillations and reversals can result from dynamo waves produced by rapidly rotating convection in a spherical shell, even in the presence of no-slip boundary conditions, provided that Ek and Pr_m are sufficiently small. Dynamo waves are apparently a very robust phenomenon, relevant to dynamos across a range of planetary[25–27] and astrophysical[28] scenarios. A common aspect of such dynamos is that they possess a relatively large toroidal magnetic field, obtained by stretching due to differential rotation. Strong azimuthal fields just outside the tangent cylinder, which are related to an omega effect taking place at this location, are a characteristic feature of the reversing dynamos reported here.

Our more Earth-like parameter regime brings further surprises. The conventional wisdom is that the local Rossby number Ro_l (see Methods) is important for delineating two regimes of behaviour[7]: for $Ro_l < 0.1$ the dynamos are generally dipolar and of stable polarity, whereas, as the driving is increased and inertial effects play a more important part, the dynamos become multipolar and reversing[29–32]. In these previous studies, the dynamos have viscous and Ohmic diffusivities that are broadly similar ($Pr_m = \mathcal{O}(1)$). S6, with its small Pr_m and Ek, has $Ro_l = 0.06$ (Extended Data Table 2) and so contradicts the accepted regime division by lying in the purportedly stable dipolar regime. Similarly, our dynamo S6 should lie close to the non-reversing regime ($Ro_l < 0.05$) according to a study of magnetic reversal frequency scaling[8]. Conversely, it exhibits a reversal frequency that is predicted to occur only at $Ro_l = 0.4$ according to dynamos for which $Ek > 3\times10^{-4}$ and $3 \le Pr_m \le 20$.

The polarity reversals exhibited by S6 are nearly periodic, but if the Rayleigh number is increased, for example, as in S6.07, the time dependence becomes more variable, and Earth-like events such as dipole excursions become possible (Extended Data Fig. 2). Moreover, at a radius corresponding to Earth's surface, the field in S6 is dipole-dominated between reversals (Supplementary Video 7). Our results therefore indicate that dynamo waves could indeed play a part in long-term geomagnetic variability[2,33]. Unfortunately, it is currently a huge computational undertaking to produce the long time series needed to fully characterize the statistics of reversals in the low-Ek regime: S6 required 4×10^6 CPU hours (approximately 457 CPU years) to integrate for 6.5 magnetic diffusion times. More complete studies of the dynamics of polarity reversals in dynamos at low viscosity may therefore have to wait for new numerical tools that are capable of more efficiently exploring this challenging regime.

Online Content Methods, along with any additional Extended Data display items and Source Data, are available in the online version of the paper; references unique to these sections appear only in the online paper.

Received 1 February; accepted 2 September 2016.
Published online 7 November 2016.

1. Moffatt, H. K. *Field Generation in Electrically Conducting Fluids* (Cambridge Univ. Press, 1978).
2. Parker, E. N. *Cosmical Magnetic fields: Their Origin and Their Activity* (Oxford Univ. Press, 1979).
3. Jacobs, J. A. *Reversals of the Earth's Magnetic Field* (Cambridge Univ. Press, 1994).
4. Merrill, R. T. & McFadden, P. L. Geomagnetic polarity transitions. *Rev. Geophys.* **37,** 201–226 (1999).

© 2016 Macmillan Publishers Limited, part of Springer Nature. All rights reserved.

5. Pétrélis, F. & Fauve, S. Mechanisms for magnetic field reversals. *Philos. Trans. R. Soc. Lond. A* **368,** 1595–1605 (2010).
6. Olson, P., Driscoll, P. & Amit, H. Dipole collapse and reversal precursors in a numerical dynamo. *Phys. Earth Planet. Inter.* **173,** 121–140 (2009).
7. Christensen, U. & Aubert, J. Scaling properties of convection-driven dynamos in rotating spherical shells and application to planetary magnetic fields. *Geophys. J. Int.* **166,** 97–114 (2006).
8. Olson, P. & Amit, H. Magnetic reversal frequency scaling in dynamos with thermochemical convection. *Phys. Earth Planet. Inter.* **229,** 122–133 (2014).
9. Parker, E. N. Hydromagnetic dynamo models. *Astrophys. J.* **122,** 293–314 (1955).
10. Busse, F. H. & Simitev, R. D. Parameter dependences of convection-driven dynamos in rotating spherical fluid shells. *Geophys. Astrophys. Fluid Dyn.* **100,** 341–361 (2006).
11. Christensen, U. R. & Wicht, J. in *Treatise on Geophysics* 2nd edn (ed. Schubert, G.) Vol. 8, 245–277 (Elsevier, 2015).
12. Roberts, P. H. & King, E. M. On the genesis of the Earth's magnetism. *Rep. Prog. Phys.* **76,** 096801 (2013).
13. Kida, S., Araki, K. & Kitauchi, H. Periodic reversals of magnetic field generated by thermal convection in a rotating spherical shell. *J. Phys. Soc. Jpn* **66,** 2194–2201 (1997).
14. Sarson, G. R. Reversal models from dynamo calculations. *Philos. Trans. R. Soc. Lond. A* **358,** 921–942 (2000).
15. Amit, H., Leonhardt, R. & Wicht, J. Polarity reversals from paleomagnetic observations and numerical dynamo simulations. *Space Sci. Rev.* **155,** 293–335 (2010).
16. Wicht, J. & Olson, P. A detailed study of the polarity reversal mechanism in a numerical dynamo model. *Geochem. Geophys. Geosyst.* **5,** Q03H10 (2004).
17. Glatzmaier, G. A. Geodynamo simulations—how realistic are they? *Annu. Rev. Earth Planet. Sci.* **30,** 237–257 (2002).
18. Busse, F. & Simitev, R. Toroidal flux oscillation as possible cause of geomagnetic excursions and reversals. *Phys. Earth Planet. Inter.* **168,** 237–243 (2008).
19. Roberts, P. H. Kinematic dynamo models. *Philos. Trans. R. Soc. Lond. A* **272,** 663–698 (1972).
20. Gubbins, D. & Gibbons, S. Three-dimensional dynamo waves in a sphere. *Geophys. Astrophys. Fluid Dyn.* **96,** 481–498 (2002).
21. Sakuraba, A. & Roberts, P. H. Generation of a strong magnetic field using uniform heat flux at the surface of the core. *Nat. Geosci.* **2,** 802–805 (2009).
22. Sakuraba, A. & Roberts, P. H. in *The Earth's Magnetic Interior* (eds Petrovský, E. et al.) 117–129 (Springer, 2011).
23. Coe, R. S. & Glatzmaier, G. A. Symmetry and stability of the geomagnetic field. *Geophys. Res. Lett.* **33,** L21311 (2006).
24. Pétrélis, F., Fauve, S., Dormy, E. & Valet, J.-P. Simple mechanism for reversals of Earth's magnetic field. *Phys. Rev. Lett.* **102,** 144503 (2009).
25. Gastine, T., Duarte, L. & Wicht, J. Dipolar versus multipolar dynamos: the influence of the background density stratification. *Astron. Astrophys.* **546,** A19 (2012).
26. Jones, C. A dynamo model of Jupiter's magnetic field. *Icarus* **241,** 148–159 (2014).
27. Dietrich, W., Schmitt, D. & Wicht, J. Hemispherical Parker waves driven by thermal shear in planetary dynamos. *Europhys Lett.* **104,** 49001 (2013).
28. Dubé, C. & Charbonneau, P. Stellar dynamos and cycles from numerical simulations of convection. *Astrophys. J.* **775,** 69 (2013).
29. Kutzner, C. & Christensen, U. From stable dipolar towards reversing numerical dynamos. *Phys. Earth Planet. Inter.* **131,** 29–45 (2002).
30. Olson, P. & Christensen, U. R. Dipole moment scaling for convection-driven planetary dynamos. *Earth Planet. Sci. Lett.* **250,** 561–571 (2006).
31. Schrinner, M., Petitdemange, L. & Dormy, E. Dipole collapse and dynamo waves in global direct numerical simulations. *Astrophys. J.* **752,** 121 (2012).
32. Oruba, L. & Dormy, E. Transition between viscous dipolar and inertial multipolar dynamos. *Geophys. Res. Lett.* **41,** 7115–7120 (2014).
33. Gubbins, D. Mechanism for geomagnetic polarity reversals. *Nature* **326,** 167–169 (1987).

Supplementary Information is available in the online version of the paper.

Acknowledgements We acknowledge the computational resources provided by the Centro Svizzero di Calcolo Scientifico (CSCS) under the project s577. We are grateful to J. M. Favre from CSCS for assistance with high-performance visualization. We thank A. Willis for developing the original dynamo code that was used for the calculations reported here, and P. Marti for subsequent optimizations for the CSCS Cray. This work was partially supported by ERC grant no. 247303 (MFECE) to A.J. and by the Danish Council for Independent Research (DFF) grant no. 4002-00366 to C.C.F.

Author Contributions A.S. carried out the numerical geodynamo simulations and analysed the runs, C.C.F. drafted the manuscript and participated in the analysis of the results. All authors contributed equally to the design of the study, discussed the results, and commented on the manuscript.

Author Information Reprints and permissions information is available at www.nature.com/reprints. The authors declare no competing financial interests. Readers are welcome to comment on the online version of the paper. Correspondence and requests for materials should be addressed to A.S. (andrei.sheiko@erdw.ethz.ch).

Reviewer Information *Nature* thanks P. Olson and the other anonymous reviewer(s) for their contribution to the peer review of this work.

© 2016 Macmillan Publishers Limited, part of Springer Nature. All rights reserved.

METHODS

Governing equations and non-dimensionalization. We adopt the Boussinesq approximation for convection-driven, rotating magnetohydrodynamics, which results in the following non-dimensional equations:

$$\left(\mathrm{Ro}\frac{\partial}{\partial t}-\mathrm{Ek}\nabla^2\right)\boldsymbol{u}=\boldsymbol{N}_u-\boldsymbol{\nabla}\hat{P}$$
$$\left(\frac{\partial}{\partial t}-\nabla^2\right)\boldsymbol{B}=\boldsymbol{\nabla}\times(\boldsymbol{u}\times\boldsymbol{B})$$
$$\left(\frac{\partial}{\partial t}-q\nabla^2\right)T=\varepsilon-\boldsymbol{u}\cdot\boldsymbol{\nabla}T$$

where

$$\boldsymbol{N}_u=\mathrm{Ro}\boldsymbol{u}\times(\boldsymbol{\nabla}\times\boldsymbol{u})+(\boldsymbol{\nabla}\times\boldsymbol{B})\times\boldsymbol{B}+q\mathrm{Ra}T\boldsymbol{r}-\hat{\boldsymbol{z}}\times\boldsymbol{u}$$

The variables $\boldsymbol{u}$, $\boldsymbol{B}$ and T are the velocity, magnetic field and temperature, respectively. $\boldsymbol{\nabla}\hat{P}$ is the modified pressure that contains information about conservative forces. The axis of rotation of the system is z and $\hat{\boldsymbol{z}}$ is a unit vector in that direction. Time is denoted as t. A uniform heat source ε is included. Solenoidal conditions $\boldsymbol{\nabla}\cdot\boldsymbol{B}=0$ and $\boldsymbol{\nabla}\cdot\boldsymbol{u}=0$ are integrated into the solution technique through use of a poloidal-toroidal decomposition of the vector field. The non-dimensional parameters are

$$\begin{aligned}\mathrm{Ro}&=\eta/(2\Omega d^2)\\ \mathrm{Ek}&=\nu/(2\Omega d^2)\\ \mathrm{Ra}&=g\alpha\Delta T d/(2\Omega\kappa)\\ q&=\kappa/\eta\end{aligned}\qquad(2)$$

where Ro is the magnetic Rossby number, Ek is the Ekman number, Ra is the modified Rayleigh number and q is the Roberts number.

The units of length, time, magnetic field and temperature for the non-dimensional governing equations are chosen as

$$r\to dr,\quad t\to(d^2/\eta)t,\quad B\to(2\Omega\rho_0\mu_0\eta)^{1/2}B,\quad T\to\Delta TT,\quad d=r_\mathrm{o}-r_\mathrm{i}$$

The following symbols denote the parameters of the system: $\boldsymbol{\Omega}=\Omega\hat{\boldsymbol{z}}$ is the rotation rate, μ_0 is the permeability of free space, ρ_0 is the density, ν, κ and η are the kinematic viscosity, thermal diffusivity and magnetic diffusivity, respectively, α is the thermal expansivity and d is the thickness of the spherical shell of convecting fluid. The unit of temperature ΔT is chosen to be $\beta d/\beta^*$, where β and $\beta^*=-2(1-r_\mathrm{i}/r_\mathrm{o})$ are the dimensional and non-dimensional temperature gradients at the core–mantle boundary (CMB), respectively, and $r_\mathrm{i,o}$ are the inner and outer radii of the shell, respectively. Gravity is assumed to vary linearly with radius and has value g on the outer boundary. The spherical coordinates are denoted (r,θ,φ).

Boundary conditions and internal heating. The modelled fluid is enclosed in a rotating spherical shell between radii r_i and r_o with $c=r_\mathrm{i}/r_\mathrm{o}=0.35$. Both boundaries are no-slip and impermeable. The outer boundary is electrically insulating, the inner core has the same electrical conductivity as the outer core. In case S6_InsIC the inner core is insulating. The inner-core temperature is kept constant at $T=\frac{c^2+c+2}{2(1-c)c}$; the gradient of the temperature on the outer boundary is $\beta^*=-2/(1-c)$. A uniform heat source with $\varepsilon=3q$ is adopted throughout the outer core. In run $\mathrm{S6}_{\varepsilon0}$, the uniform heat source ε is set to zero.

Diagnostics. The dipole latitude is calculated as $\arcsin\left[g_1^0/\sqrt{\left(g_1^0\right)^2+\left(g_1^1\right)^2+\left(h_1^1\right)^2}\right]$, where $\left\{g_1^0,g_1^1,h_1^1\right\}$ are the first three Gauss coefficients of the magnetic field at the outer boundary. The kinetic and magnetic energies are defined as $E_\mathrm{kin}=\frac{1}{2}\int u^2\mathrm{d}V$ and $E_\mathrm{mag}=\frac{1}{2\mathrm{Ro}}\int B^2\mathrm{d}V$, where the volume integral is over the entire outer core. The local Rossby number[8] is defined as $\mathrm{Ro_l}=2\frac{l_u}{\pi}\mathrm{RoRe_m}$; the magnetic Reynolds number $\mathrm{Re_m}$ is Ud/η; $l_u=\frac{\sum u_l^2 l}{2E_\mathrm{kin}}$ is the mean harmonic degree; $u_l^2/2$ is the kinetic energy per harmonic degree l; $U=\sqrt{2E_\mathrm{kin}/V}$; and V is the volume of the spherical shell.

Numerical set-up. We solve the governing equations using a parameterization in spherical harmonics up to degree and order 255 for the angular component and 528 finite-difference points in radius. A second-order predictor–corrector scheme is used for the time integration[34]. The time-step is adaptive and varies throughout the run. In the case S6, the time-step started from 10^{-7} magnetic diffusion times at the initial stage of the run with a very turbulent flow, and later increased up to 2.5×10^{-6} magnetic diffusion times during the reversing interval. Parallelization is carried out in radius. In the linear parts of the code, data are split over the spherical harmonics. 528 cores were used simultaneously for one simulation.

The bulk of the simulations and visualizations were performed on the supercomputer Piz Daint (Cray XC 30) at the Swiss National Supercomputing Centre. The code was originally developed by Willis[35] and then subsequently optimized for the Cray XC 30 and successfully benchmarked against other dynamo codes[36].

Importance of the heating mode. We carried out an additional simulation $\mathrm{S6}_{\varepsilon0}$ to test how the particular choice of the internal homogeneous heating influences the reversing behaviour. In the two runs S6 and $\mathrm{S6}_{\varepsilon0}$, the internal heating ε is set to $3q$ and 0, respectively. Other parameters are the same. The run $\mathrm{S6}_{\varepsilon0}$ was started from S6. As a consequence of changing the heating mode, the temperature drop between the inner core boundary (ICB) and the CMB is modified (see Extended Data Fig. 3). An important transient effect is the secular cooling that can be defined as the decrease in the thermal energy in the shell per unit time: $Q_\mathrm{sec}=-\int_V\frac{\partial T}{\partial t}\mathrm{d}V$ (to evaluate Q_sec, the mean radial temperature gradient on the ICB is measured; see Equation (5) and Extended Data Fig. 4). We plot the ratio $Q_\mathrm{sec}/Q_\mathrm{i}^0$ of the secular cooling to the heat coming from the ICB in the steady ($Q_\mathrm{sec}=0$) state in Extended Data Fig. 5. In the modified run $\mathrm{S6}_{\varepsilon0}$, Q_sec constitutes less than 5% of the heat flux Q_i^0 from the ICB during the final magnetic diffusion time. So, we conclude that the contribution of the secular cooling term to the heat flux equation is small at this stage.

The reversal period in $\mathrm{S6}_{\varepsilon0}$ increased by less than 5% in comparison with that in S6 (see dipole latitude time dependencies for both runs in Extended Data Fig. 6). This test suggests that the inclusion or not of the internal heating term is not crucial to the dynamo-wave reversals exhibited by our dynamos. Changes in the internal heating term do nevertheless slightly alter the value of the reversal period obtained.

Volume-integrated terms of the heat equation. The heat flux equation is

$$\left(\frac{\partial}{\partial t}-q\nabla^2\right)T=\varepsilon-\boldsymbol{u}\cdot\boldsymbol{\nabla}T$$

In a quasi-stationary state $\int_V\frac{\partial T}{\partial t}\mathrm{d}V=0$, if no-slip boundary conditions ($u_\varphi=u_\theta=0$) are applied, then

$$\int_V\boldsymbol{u}\cdot\boldsymbol{\nabla}T\mathrm{d}V=\int_{\partial V}\boldsymbol{u}T\cdot\mathrm{d}\boldsymbol{S}=0$$

and the integrated heat flux equation is

$$-q\int_{r_\mathrm{i}}\frac{\partial T}{\partial r}\bigg|_{r_\mathrm{i}}\mathrm{d}S+\varepsilon V=-q\int_{r_\mathrm{o}}\frac{\partial T}{\partial r}\bigg|_{r_\mathrm{o}}\mathrm{d}S$$

This is equivalent to $Q_\mathrm{i}+Q_\mathrm{int}=Q_\mathrm{o}$, whereby the sum of the heat supplied by internal heating Q_int and that from the inner core Q_i is equal to the heat leaving through the outer boundary Q_o.

The temperature gradient at the CMB was held fixed at $\beta^*=\frac{\partial T}{\partial r}\Big|_{r_\mathrm{o}}=-2/(1-c)$, with $c=r_\mathrm{i}/r_\mathrm{o}=0.35$. In S6 the internal heating $Q_\mathrm{int}=3qV$. The heat leaving through the outer boundary $Q_\mathrm{o}=-4q\pi r_\mathrm{o}^2\beta^*$. The temperature gradient on the ICB in run S6 is

$$\frac{\partial T}{\partial r}\bigg|_{r_\mathrm{i}}=-(Q_\mathrm{o}-Q_\mathrm{int})/(4q\pi r_\mathrm{i}^2)=\frac{\beta^*}{c^2}+\left(\frac{1}{c^3}-1\right)r_\mathrm{i}=-13.1\qquad(3)$$

In the case $\mathrm{S6}_{\varepsilon0}$ without internal heating, the temperature gradient at r_i is

$$\frac{\partial T}{\partial r}\bigg|_{r_\mathrm{i}}=-Q_\mathrm{o}/(4q\pi r_\mathrm{i}^2)=\frac{\beta^*}{c^2}=-25.1\qquad(4)$$

Without internal heating, in a steady case the heat from the ICB goes through the shell and leaves without losses or gains at the CMB. The power flowing through the CMB and the ICB is equal, although the heat flux is smaller at the CMB because it is inversely proportional to the surface area, yielding the coefficient $(r_\mathrm{o}/r_\mathrm{i})^2=1/c^2$ in equation (4).

Let us consider the non-steady case:

$$Q_\mathrm{i}+Q_\mathrm{int}=Q_\mathrm{o}+\int_V\frac{\partial T}{\partial t}\mathrm{d}V$$

where $Q_\mathrm{sec}=-\int_V\frac{\partial T}{\partial t}\mathrm{d}V$ is the secular cooling. If the heat flux from the inner core in the steady case is Q_i^0, the $Q_\mathrm{sec}=Q_\mathrm{i}^0-Q_\mathrm{i}$. So, the difference between the steady state and the actual value of the heat flux from the inner boundary is the secular cooling. The relative influence of the secular cooling can be calculated as

$$Q_\mathrm{sec}/Q_\mathrm{i}^0=1-Q_\mathrm{i}/Q_\mathrm{i}^0\qquad(5)$$

© 2016 Macmillan Publishers Limited, part of Springer Nature. All rights reserved.

34. Sheyko, A. *Numerical Investigations of Rotating MHD in a Spherical Shell*. PhD thesis, ETH Zürich, 24–26 (2014); http://e-collection.library.ethz.ch/view/eth:9016.
35. Willis, A. P., Sreenivasan, B. & Gubbins, D. Thermal core–mantle interaction: exploring regimes for locked dynamo action. *Phys. Earth Planet. Inter.* **165,** 83–92 (2007).
36. Jackson, A. *et al.* A spherical shell numerical dynamo benchmark with pseudo-vacuum magnetic boundary conditions. *Geophys. J. Int.* **196,** 712–723 (2014).
37. Rotvig, J. An investigation of reversing numerical dynamos driven by either differential or volumetric heating. *Phys. Earth Planet. Inter.* **176,** 69–82 (2009).
38. Driscoll, P. & Olson, P. Effects of buoyancy and rotation on the polarity reversal frequency of gravitationally driven numerical dynamos. *Geophys. J. Int.* **178,** 1337–1350 (2009).
39. Takahashi, F., Matsushima, M. & Honkura, Y. A numerical study on magnetic polarity transition in an MHD dynamo model. *Earth Planets Space* **59,** 665–673 (2007).
40. Olson, P. & Deguen, R. Eccentricity of the geomagnetic dipole caused by lopsided inner core growth. *Nat. Geosci.* **5,** 565–569 (2012).
41. Wicht, J., Stellmach, S. & Harder, H. in *Geomagnetic Field Variations* (eds Glaßmeier, K.-H. et al.) 107–158 (Springer, 2009).
42. Aubert, J., Aurnou, J. & Wicht, J. The magnetic structure of convection-driven numerical dynamos. *Geophys. J. Int.* **172,** 945–956 (2008).
43. Sreenivasan, B., Sahoo, S. & Dhama, G. The role of buoyancy in polarity reversals of the geodynamo. *Geophys. J. Int.* **199,** 1698–1708 (2014).

© 2016 Macmillan Publishers Limited, part of Springer Nature. All rights reserved.

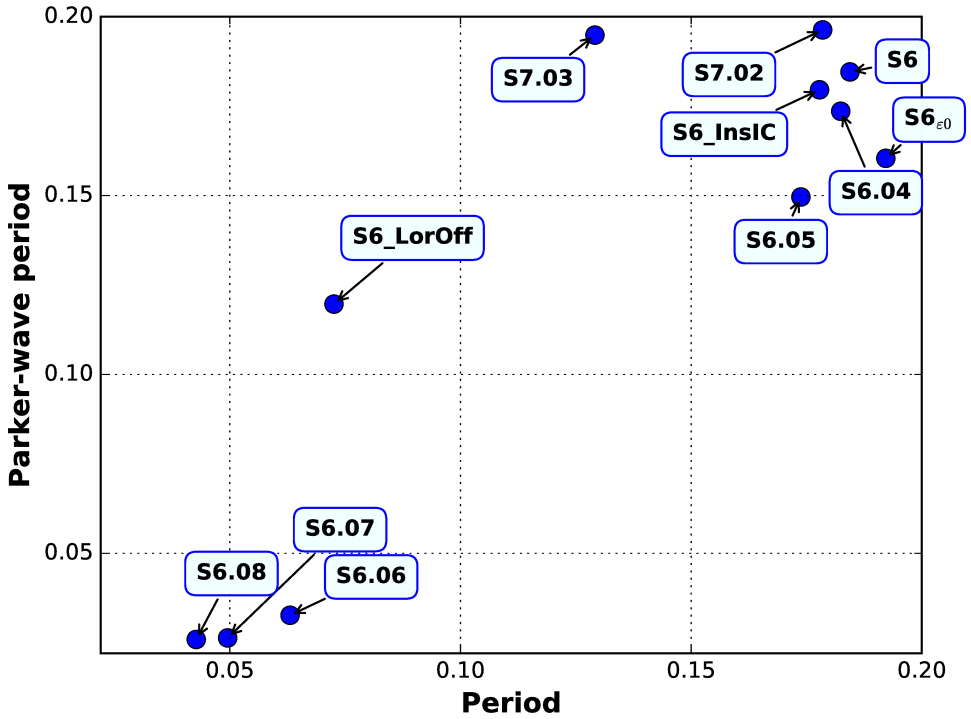

Extended Data Figure 1 | Systematics of reversal period versus dynamo-wave predictions. Comparison of the scaling of periods predicted by Parker's dynamo-wave theory (Equation (1)) and the periods obtained in the dynamo calculations. Periods in the numerical calculations are determined from spectral analysis of the time series of dipole latitudes. The predicted periods from Parker's dynamo-wave theory are calculated from volume-averaged helicity and zonal toroidal kinetic energy time-averaged over the last three reversals in the simulation or, in shorter simulations, during the second half of the reversing interval, with $\gamma = 200$ (Equation (1)). Numerical values of measured and estimated periods are provided in Extended Data Table 2.

© 2016 Macmillan Publishers Limited, part of Springer Nature. All rights reserved.

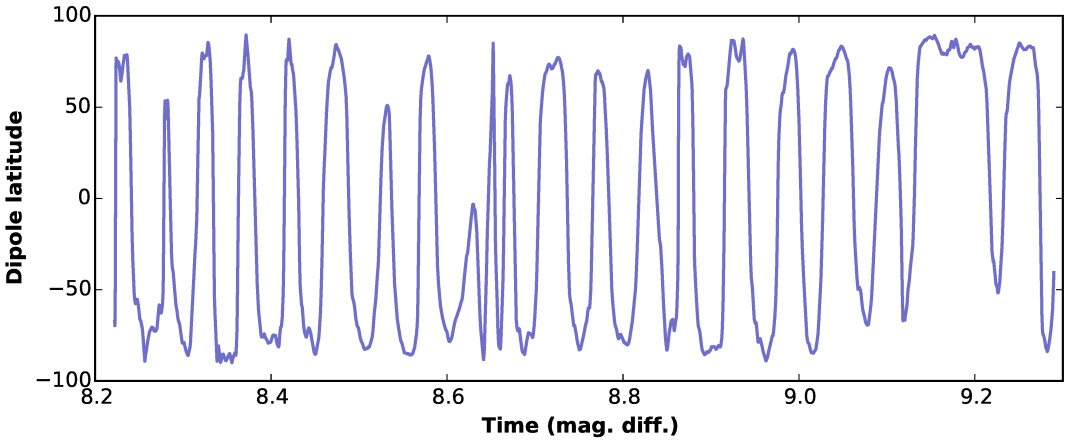

Extended Data Figure 2 | Time dependence of dipole tilt for dynamo S6.07. The time dependence of the dipole tilt, determined from the first three Gauss coefficients $\{g_1^0, g_1^1, h_1^1\}$ of the magnetic field at the outer boundary. Units are magnetic diffusion times. S6.07 was started from a previous run S6.06, and then the Rayleigh number Ra was increased by a factor of two.

© 2016 Macmillan Publishers Limited, part of Springer Nature. All rights reserved.

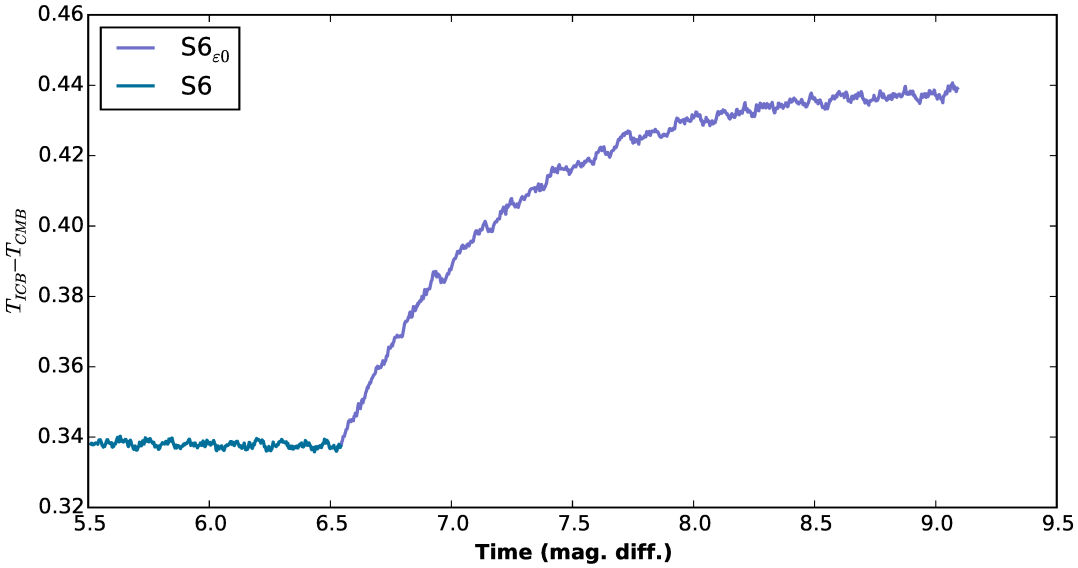

Extended Data Figure 3 | The temperature drop between the ICB and the CMB in runs S6 and S6$_{\varepsilon 0}$. Run S6$_{\varepsilon 0}$ starts from S6; the temperature drop increases after the internal heating is switched off.

© 2016 Macmillan Publishers Limited, part of Springer Nature. All rights reserved.

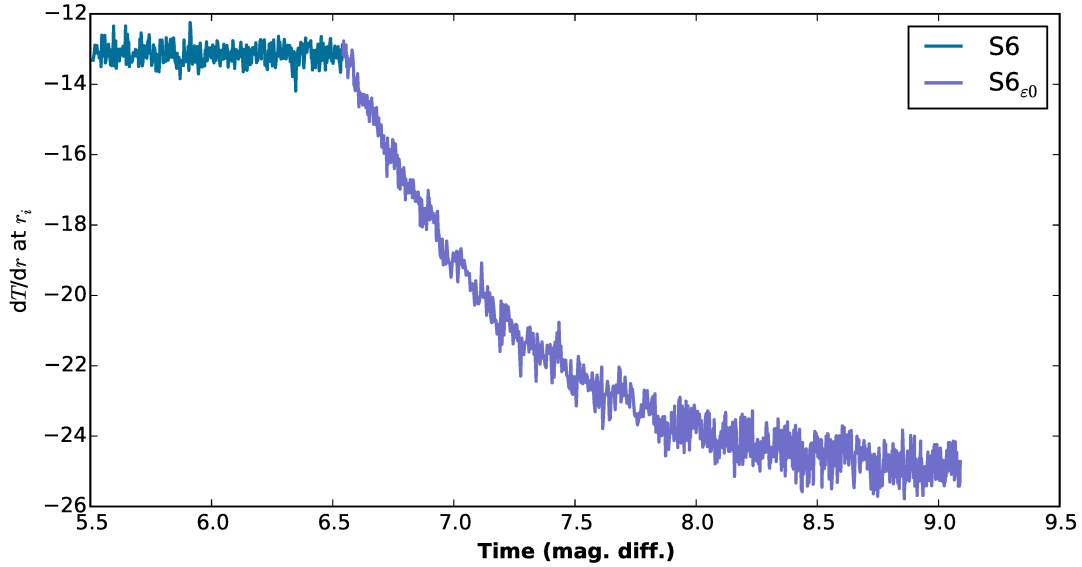

Extended Data Figure 4 | Radial temperature gradient on the ICB in runs S6 and S6$_{\varepsilon 0}$. Steady-state values are −13.1 and −25.1 for runs S6 and S6$_{\varepsilon 0}$, respectively (see Equations (3) and (4)).

© 2016 Macmillan Publishers Limited, part of Springer Nature. All rights reserved.

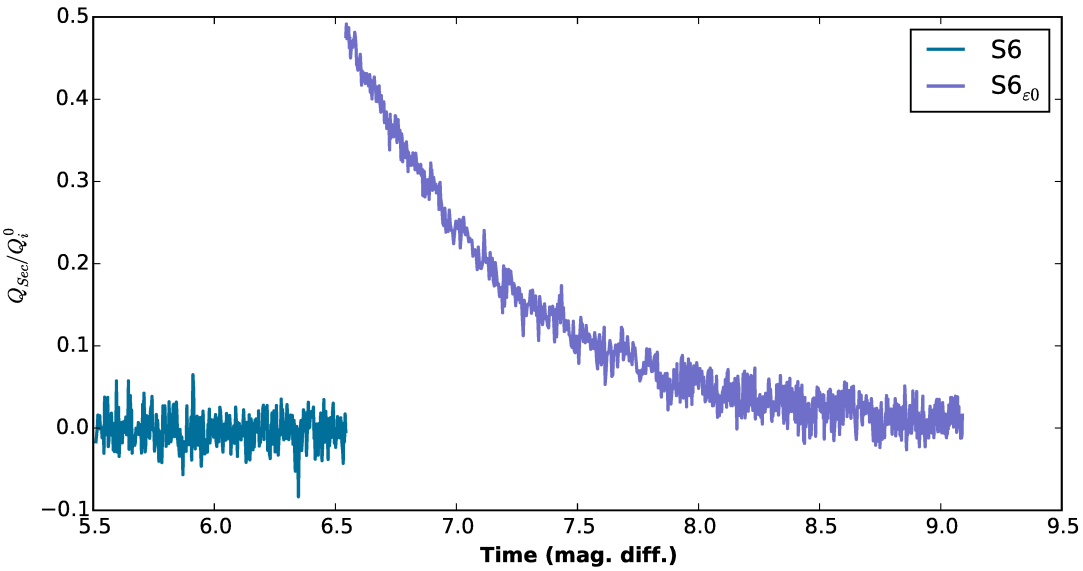

Extended Data Figure 5 | Secular cooling normalized by the steady-state heat flux through the CMB (see Equation (5)), for runs S6 and S6$_{\varepsilon 0}$.

© 2016 Macmillan Publishers Limited, part of Springer Nature. All rights reserved.

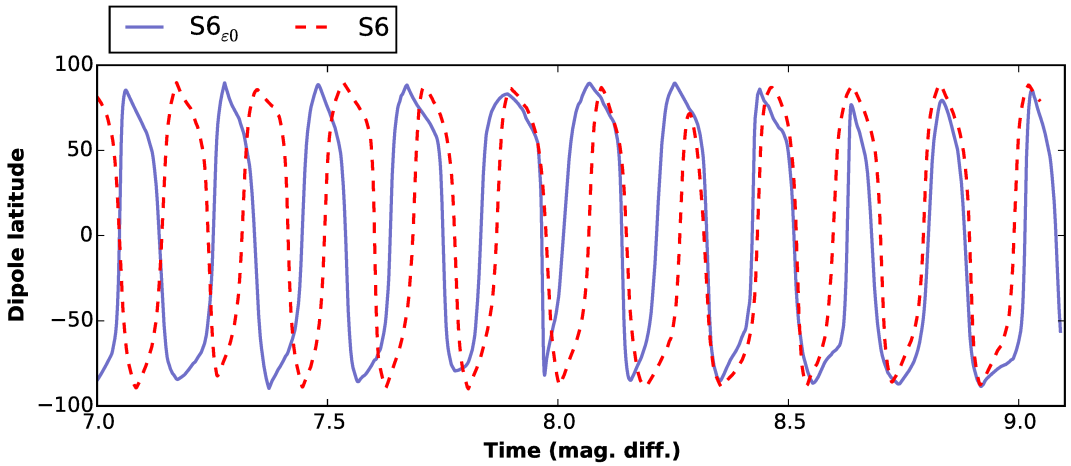

Extended Data Figure 6 | Time dependence of dipole latitude for dynamos S6 and S6$_{\varepsilon 0}$. The plot for S6 is shifted along the time axis to overlap S6$_{\varepsilon 0}$.

© 2016 Macmillan Publishers Limited, part of Springer Nature. All rights reserved.

Extended Data Table 1 | Selection of previous geodynamo model reversal studies included in Fig. 1

Ek	$Pr_m = Ek/Ro$	Author
$\mathcal{O}(10^{-15})$	$\mathcal{O}(10^{-5})$	Earth
$10^{-3} - 10^{-4}$	0.67–6	Kutzner and Christensen (2002)[29]
$10^{-2} - 3 \times 10^{-4}$	20	Rotvig (2009)[37]
5×10^{-3}	20	Driscoll and Olson (2009)[38]
6.5×10^{-3}	20	Olson et al. (2009)[6]
10^{-5}	0.5	Takahashi et al. (2007)[39]
10^{-2}	20	Wicht and Olson (2004)[16]
6×10^{-3}	20	Olson and Deguen (2012)[40]
$2 \times 10^{-2} - 3 \times 10^{-4}$	3–10	Wicht et al. (2009)[41]
10^{-5}	0.5	Busse and Simitev (2008)[18]
$2 \times 10^{-2} - 3 \times 10^{-4}$	3–10	Aubert et al. (2008)[42]
1.1×10^{-2}	10	Kida et al. (1997)[13]
3×10^{-4}	5	Sreenivasan et al. (2014)[43]
1.1834×10^{-6}	0.04–0.05	Present study

We list two of the important control parameters, the magnetic Prandtl number Pr_m and the Ekman number Ek. Our aim was to make Pr_m substantially less than unity and to decrease the smallest previously reported value for Ek by at least an order of magnitude. Values from previous studies are from refs 6, 13, 16, 18, 29, 37–43.

© 2016 Macmillan Publishers Limited, part of Springer Nature. All rights reserved.

Extended Data Table 2 | Runs exploring variation of reversals with control parameters and set-up

	Ek	Ro	Ra	q	Re_m	Ro_l	E_{kin}/E_{mag}	$\overline{E_{tor}}$	H	T_{osc}	T_{Parker}
S6	1.1834e-06	2.3669e-05	6591	0.050	89	0.064	9.22	5.08e+03	6.51e+05	0.184	0.185
S6.04	1.1834e-06	2.3669e-05	7250	0.050	94	0.071	8.93	5.65e+03	6.98e+05	0.182	0.174
S6.05	1.1834e-06	2.3669e-05	10000	0.050	105	0.084	6.53	6.98e+03	8.45e+05	0.174	0.150
S6.06	1.1834e-06	2.3669e-05	100000	0.050	333	0.226	3.22	9.19e+04	4.88e+06	0.063	0.033
S6.07	1.1834e-06	2.3669e-05	200000	0.050	388	0.258	2.91	1.40e+05	6.08e+06	0.050	0.026
S6.08	1.1834e-06	2.3669e-05	250000	0.050	396	0.286	3.06	1.40e+05	6.30e+06	0.043	0.026
S7.02	1.1834e-06	2.6299e-05	6591	0.045	84	0.066	12.56	5.73e+03	5.41e+05	0.178	0.196
S7.03	1.1834e-06	2.9586e-05	6591	0.040	83	0.065	31.23	8.15e+03	4.61e+05	0.129	0.195
S6_InsIC	1.1834e-06	2.3669e-05	6591	0.050	91	0.066	10.27	5.57e+03	6.56e+05	0.178	0.180
S6_LorOff	1.1834e-06	2.3669e-05	6591	0.050	119	0.061	–	2.54e+04	6.92e+05	0.073	0.120
$S6_{\varepsilon 0}$	1.1834e-06	2.3669e-05	6591	0.050	100	0.076	6.12	6.00e+03	7.92e+05	0.192	0.160

T_{osc} is the period of reversals determined from spectral analysis of the model dipole tilt time series. T_{Parker} is the period of reversals determined by Equation (1) with $\gamma = 200$. $\overline{E_{tor}}$ is the energy of the axially symmetric component of the toroidal flow. H is the modulus of the volume-integrated kinetic helicity of the non-axisymmetric flow in the northern hemisphere. Definitions of other parameters and diagnostics are provided in Methods. Presented diagnostics are averaged over the last three reversals or, in shorter simulations, during the second half of the reversing interval.

© 2016 Macmillan Publishers Limited, part of Springer Nature. All rights reserved.